INTERNATIONAL JOURNAL FOR NUMERICAL METHODS IN FLUIDS
Int. J. Numer. Meth. Fluids 2004; **45**:231–252 (DOI: 10.1002/fld.664)

Simulation of two-dimensional turbulent flows in a rotating annulus

Brian D. Storey*

Franklin W. Olin College of Engineering, Olin Way, Needham, MA 02492-1245, U.S.A.

SUMMARY

Rotating water tank experiments have been used to study fundamental processes of atmospheric and geophysical turbulence in a controlled laboratory setting. When these tanks are undergoing strong rotation the forced turbulent flow becomes highly two dimensional along the axis of rotation. An efficient numerical method has been developed for simulating the forced quasi-geostrophic equations in an annular geometry to model current laboratory experiments. The algorithm employs a spectral method with Fourier series and Chebyshev polynomials as basis functions. The algorithm has been implemented on a parallel architecture to allow modelling of a wide range of spatial scales over long integration times. This paper describes the derivation of the model equations, numerical method, testing and performance of the algorithm. Results provide reasonable agreement with the experimental data, indicating that such computations can be used as a predictive tool to design future experiments. Copyright © 2004 John Wiley & Sons, Ltd.

KEY WORDS: atmospheric fluid dynamics; rotating flows; spectral methods

1. INTRODUCTION

Under strong rotation, fluid flows tend to become two dimensional along the axis of rotation due to the influence of the Coriolis force. Two dimensionalization is expected when the fluid vorticity is small compared to the rate of system rotation. Flows of atmospheres and oceans, where structures are large and velocities slow, are often dominated by the Coriolis force [1].

In order to study the underlying processes of rotating two-dimensional flows, numerous lab experiments have been conducted in rapidly rotating tanks. This paper will focus on the experimental apparatus at the University of Texas at Austin that has been used to generate results found in References [2–8]. This particular experimental arrangement has been used to generate two-dimensional jets and vortices that model atmospheric processes as well as measure statistics of two-dimensional turbulence. Past experiments were used to model eastward

*Correspondence to: B. D. Storey, Franklin W. Olin College of Engineering, Olin Way, Needham, MA 02492-1245, U.S.A.

Contract/grant sponsor: NPACI program of NSF

Received 3 February 2003
Revised 3 October 2003

and westward atmospheric jets and long-lived vortices such as Jupiter's Great Red Spot [2–4]. Current experiments have focused on computing the turbulent statistics of these nearly two-dimensional flows. For example, experimental results have shown evidence of a k^{-2} turbulent energy spectrum rather than the typical $k^{-5/3}$ Kolmogorov spectrum [5]. Other experiments have shown success in predicting probability distribution functions using non-extensive statistical mechanics [6]. We would like to use numerical simulation to complement experimental results in order to develop a more complete understanding of these statistics. In addition to using the numerical simulations to explain past results we would like to use the numerical simulations to help design future laboratory set-ups by predicting system behaviour without rebuilding the experimental apparatus.

The laboratory system consists of water inside an enclosed annular ring with a 10.8 cm inner radius and 43.2 cm outer radius. The entire apparatus can be rotated up to 2.5 Hz. The bottom of the tank has a sloping boundary (slope is -0.1) to simulate the effect of Coriolis force varying with latitude in atmospheres [1]. The mean height of the tank is 18.7 cm. Water is pumped into and out of a series of small holes located along the bottom of the tank. The vertical flow from each of these holes couples directly to the Coriolis force to generate vorticity in the rotation direction. As the vortices grow in strength they begin to advect each other around the domain, undergoing vortex merger and decay—all the while remaining two dimensional in the rotation direction.

To validate the numerical method we will compare the simulation to experimental results obtained from two different forcing configurations. The first configuration has two rings of holes that extend the circumference of the annulus. The inner ring at a radius of 18.9cm pumps water into the closed tank and the outer ring at 35.1 cm removes the water. Each ring has 120 holes where each hole is 0.25 cm in diameter. Experimental results of Reference [7] provide data from this configuration. This forcing configuration results in a strong counter-rotating jet (with respect to the tank rotation) that meanders around the annulus when observing the flow from the rotating frame. The second experiment has 120 holes in a single ring at the mean radius of 27 cm. One set of holes along a semi-circle are inlets and the other semi-circle consists of outlets. Experimental results from this forcing configuration have been documented in Reference [8]. This semi-circle forcing results in a co-rotating jet along the centre of the tank with counter-rotating jets at the inner and outer walls.

This paper will describe the derivation of the governing equations, the numerical method, algorithm performance and sample simulation results. We find that the simulation can obtain qualitative and quantitative agreement with the experimental results.

2. GOVERNING EQUATIONS

This section will review the governing equations that model the flow in the annulus. The interested reader should consult [1] for more complete details.

The conservation of momentum for the incompressible, constant viscosity fluid flow is

$$\frac{\mathrm{D}u}{\mathrm{D}t} + fv = -\frac{1}{\rho r}\frac{\partial P}{\partial \theta} + \nu\left(\nabla^2 u - \frac{u}{r^2} + \frac{2}{r^2}\frac{\partial v}{\partial \theta}\right) \tag{1}$$

$$\frac{\mathrm{D}v}{\mathrm{D}t} - fu = -\frac{1}{\rho}\frac{\partial P}{\partial r} + \nu\left(\nabla^2 v - \frac{v}{r^2} - \frac{2}{r^2}\frac{\partial u}{\partial \theta}\right) \tag{2}$$

$$\frac{\mathrm{D}w}{\mathrm{D}t} = -\frac{1}{\rho}\frac{\partial P}{\partial z} + \nu\nabla^2 w \tag{3}$$

where u, v and w are the velocity components in the three co-ordinate directions, θ, r and z. P is the pressure, ρ is the density of the fluid, ν is the viscosity, $\mathrm{D}/\mathrm{D}t$ is the material derivative and f is the Coriolis parameter (2Ω in the annulus). The rotation vector points in the vertical direction (z) in this laboratory experiment. The vector operators ∇^2 and $\mathbf{u}.\nabla\mathbf{u}$ (hidden in the material derivative) are written in cylindrical co-ordinates. The variable u is used to denote the θ component of the velocity since many simulations cast the annulus to a two-dimensional strip, where the θ direction is equivalent to the x direction in which is mean flow exists [9]. This notation for annular flows has been used in previous studies [10].

We will reduce these equations to a simpler set by non-dimensionalizing the equations and taking the limit of strong rotation. To non-dimensionalize the equations we use the system radius, R, the characteristic flow velocity, U_0, and the time $t_0 = R/U_0$ as the scaling parameters. When rotation rate is strong, it is known that the dominant balance in the equations occurs between the Coriolis force and the pressure. This balance can be confirmed by noting that large-scale streamlines on a weather map closely match isobars. Therefore, we non-dimensionalize the pressure by the scale,

$$P_0 = \rho f U_0 R \tag{4}$$

Using this scaling and writing the equations in non-dimensional form yields

$$Ro\frac{\mathrm{D}u}{\mathrm{D}t} + v = -\frac{1}{r}\frac{\partial P}{\partial \theta} + \frac{Ro}{Re}\left(\nabla^2 u - \frac{u}{r^2} + \frac{2}{r^2}\frac{\partial v}{\partial \theta}\right) \tag{5}$$

$$Ro\frac{\mathrm{D}v}{\mathrm{D}t} - u = -\frac{\partial P}{\partial r} + \frac{Ro}{Re}\left(\nabla^2 v - \frac{v}{r^2} - \frac{2}{r^2}\frac{\partial u}{\partial \theta}\right) \tag{6}$$

$$Ro\frac{\mathrm{D}w}{\mathrm{D}t} = -\frac{\partial P}{\partial z} + \frac{Ro}{Re}\nabla^2 w \tag{7}$$

where Re and Ro are the Reynolds ($U_0 R/\nu$) and Rossby (U_0/fR) numbers. Knowing that in turbulent flows the Reynolds number is very large (10^4 in the lab, much larger in atmospheres) we might be tempted to discard the viscous term. However, we will be interested in effects at the inner and outer boundary during the laboratory experiments, and therefore will not discard the viscous terms.

Under strong rotation the Rossby number is small, and therefore becomes the perturbation parameter. Expanding the velocity field in a series using the Rossby number (i.e. $u = u_0 + Ro\,u_1$) and taking the zero Rossby number limit yields

$$v_0 = -\frac{1}{r}\frac{\partial P_0}{\partial \theta} \tag{8}$$

$$u_0 = \frac{\partial P_0}{\partial r} \tag{9}$$

$$0 = -\frac{\partial P_0}{\partial z} \tag{10}$$

It is easy to see that applying Equation (10) to Equations (8) and (9) demands that the horizontal zero-order flows (u_0, v_0) are constant in the z direction. The above equations also show that the zero-order solution is divergence free in the r–θ plane. Since the zeroth order velocity in the horizontal plane is divergence free, the vertical velocity is invariant in the vertical direction. The rigid walls at the upper and lower boundary implies that the zeroth order vertical flow is zero.

The zeroth order solution provides interesting information but does not allow us to solve for the flow velocities. To obtain the velocities we need to proceed to the next order and collect terms of the order Ro as follows.

$$\frac{\mathrm{D}_0 u_0}{\mathrm{D}t} + v_1 = -\frac{1}{r}\frac{\partial P_1}{\partial \theta} + \frac{1}{Re}\left(\nabla^2 u_0 - \frac{u_0}{r^2} + \frac{2}{r^2}\frac{\partial v_0}{\partial \theta}\right) \tag{11}$$

$$\frac{\mathrm{D}_0 v_0}{\mathrm{D}t} - u_1 = -\frac{\partial P_1}{\partial r} + \frac{1}{Re}\left(\nabla^2 v_0 - \frac{v_0}{r^2} - \frac{2}{r^2}\frac{\partial u_0}{\partial \theta}\right) \tag{12}$$

$$\frac{\mathrm{D}_0 w_0}{\mathrm{D}t} = -\frac{\partial P_1}{\partial z} + \frac{1}{Re}\nabla^2 w_0 \tag{13}$$

where the notation $\mathrm{D}_0/\mathrm{D}t$ means the material derivative using the zero-order velocities. Since the zeroth order vertical velocity is zero, Equation (13) reduces to

$$0 = -\frac{\partial P_1}{\partial z} \tag{14}$$

Taking the derivative of Equations (11) and (12) with respect to z and using the fact that u_0 and v_0 do not depend on z and Equation (14) yields

$$\frac{\partial u_1}{\partial z} = 0 \tag{15}$$

$$\frac{\partial v_1}{\partial z} = 0 \tag{16}$$

The first-order horizontal velocities (just like the zeroth order) are invariant in the vertical direction. Strong two dimensionalization along the rotation direction is confirmed experimentally by velocity measurements that show a very strong correlation in the vertical direction of the highly turbulent flow [7].

Taking the cross derivatives of the first-order momentum equations (Equations (11), (12)) yields the vorticity equation

$$\frac{\partial \omega_0}{\partial t} + \frac{u_0}{r}\frac{\partial \omega_0}{\partial \theta} + v_0\frac{\partial \omega_0}{\partial r} + \left(\frac{1}{r}\frac{\partial u_1}{\partial \theta} + \frac{1}{r}\frac{\partial r v_1}{\partial r}\right) = \frac{1}{Re}\nabla^2 \omega_0 \tag{17}$$

where the vorticity is defined as

$$\omega_0 = \frac{1}{r}\frac{\partial r u_0}{\partial r} - \frac{1}{r}\frac{\partial v_0}{\partial \theta} \tag{18}$$

To close the zeroth order vorticity equation we apply the conservation of mass to derive an expression for the divergence in the r–θ plane of the first-order velocity field.

The conservation of mass for the fluid at order Ro is

$$\frac{1}{r}\frac{\partial u_1}{\partial \theta} + \frac{1}{r}\frac{\partial r v_1}{\partial r} + \frac{\partial w_1}{\partial z} = 0 \tag{19}$$

We stated above that the horizontal velocities are invariant in the z-direction, therefore we can integrate the continuity equation across the height of the annulus.

$$\left(\frac{1}{r}\frac{\partial u_1}{\partial \theta} + \frac{1}{r}\frac{\partial r v_1}{\partial r}\right)\frac{H}{R} = (w_1|_{z=0} - w_1|_{z=H}) \tag{20}$$

The annulus has vertical flow that is imposed by the sloping lower boundary, Ekman pumping at the upper and lower boundary, and the vertical forcing at the inlet/outlet holes. We now turn to each of these terms individually.

Since the height of the water varies as a function of radius, flow in the radial direction drives vertical flow. The vertical flow due to the bottom topography is given as

$$w|_{z=0} = \eta v_0 \tag{21}$$

where η is the slope of the bottom. Note that the vertical velocity is imposed by the geometry. The slope is assumed to be a small parameter on the order of the Rossby number (or smaller), otherwise our particular scaling might break down. The laboratory value is $\eta = -0.1$.

In addition to the velocity from the sloping boundary, viscosity in the boundary layer is known to cause a slight vertical velocity. This boundary layer vertical velocity is known as Ekman pumping and the magnitude of the velocity is given by [1]

$$w|_{z=0} - w|_{z=H} = \omega_0\sqrt{\frac{2\nu}{fR^2}} = \omega_0\sqrt{\frac{2\,Ro}{Re}} \tag{22}$$

Ekman pumping contributes a term at both the upper and lower boundary of equal magnitude where the flow is directed toward the centre height of the annulus. Whether or not an 'effective' viscosity is needed for capturing the turbulent Ekman pumping is considered in Section 4.4.

In addition to the Ekman velocity and the sloping bottom, there is also a vertical velocity imposed by the forcing jets, $W_f(r,\theta)$. The forcing velocity is localized in space at the holes which are 0.25 cm in diameter. The vertical velocity may be too high for the scaling to be valid (the vertical velocity is quite large), but we assume that the effect of the forcing is quite localized and therefore the quasi-geostrophic (QG) approximation is valid. In the experiments, the holes are only 0.25 cm in diameters while the vortices formed are several centimetres in extent.

We sum the vertical velocity terms and substitute into Equation (20) to obtain

$$\left(\frac{1}{r}\frac{\partial u_1}{\partial \theta} + \frac{1}{r}\frac{\partial r v_1}{\partial r}\right) = \frac{R}{H\,Ro}\left(\eta v_0 + \omega_0\sqrt{\frac{2\,Ro}{Re}} + W_f(r,\theta)\right) \tag{23}$$

Note that in the above expression we must remember that $w = w_0 + Ro\, w_1$, which results in the Ro term on the right-hand side of the equation.

The divergence of the horizontal velocity field (23) can be substituted into the vorticity equation (17) to yield

$$\frac{\partial \omega_0}{\partial t} + \frac{u_0}{r}\frac{\partial \omega_0}{\partial \theta} + v_0\left(\frac{\partial \omega_0}{\partial r} + \frac{\delta \eta}{Ro}\right) + \frac{\delta \omega_0}{\tau} + \frac{\delta W_f(r,\theta)}{Ro} = \frac{1}{Re}\nabla^2 \omega_0 \tag{24}$$

where $\tau = \sqrt{Re\, Ro/2}$ is the Ekman spin down time and $\delta = R/H$ is the annulus aspect ratio.

Equation (24) is one specific form of QG equation. It is easy to verify that the vorticity is related to the velocity through the streamfunction

$$\nabla^2 \Psi_0 = -\omega_0 \tag{25}$$

and the zeroth order velocity is related to the streamfunction in the usual manner. The boundary conditions that we wish to impose are no slip and no-normal velocity at the inner and outer wall of the annulus.

The QG equations are only valid in the limit of small Rossby number and the experiments provide excellent data describing the departure from two dimensionality as the Rossby number increases [7]. Using the definition $Ro = \omega_{\text{rms}}/2\Omega$, the experiments demonstrated that the $Ro < 0.2$ flow is two dimensional while flows with $Ro > 0.3$ begin to show significant three-dimensional effects. The slope of the bottom of the tank should be on the same order as the Rossby number in order to keep consistent scaling for the vertical velocity.

2.1. Forcing approximation

The forcing of the flow comes from a series of 120 small holes located at a fixed radius in the annulus. If we consider the case where the forcing ring in the laboratory experiments is located at 35 cm, then the forcing ring is 220 cm in circumference. Each of the forcing holes in the laboratory are 0.25 cm in diameter. For the case of 1024 grid points in the simulation the grid spacing is 0.2 cm at the outer forcing radius. Even at this very high resolution it will be difficult to achieve adequate resolution of individual vortices formed directly from the forcing holes.

Since there cannot be complete resolution of the forcing scales we will use an approximation developed by Marcus and Lee [10] that models the set of holes as a uniform forcing slit in the θ direction. Marcus and Lee [10] provide a formula for the width of the effective slit,

$$L^{\text{slit}} = \sqrt{H}\left(\frac{P}{8\pi N_{\text{holes}}}\right)^{1/4}\left(\frac{1}{fv}\right)^{1/8} \tag{26}$$

where P (cm^3/s) is the total pumping rate through the holes.

2.2. Summary

We summarize this section by writing the final form of the equations. We drop the 0 and 1 subscript notation for the vorticity and the streamfunction as we have only have zeroth order terms after our manipulation. The governing equation for our system, where the ∇^2 operator

is in cylindrical co-ordinates are

$$\frac{\partial\omega}{\partial t}+\frac{u}{r}\frac{\partial\omega}{\partial\theta}+v\left(\frac{\partial\omega}{\partial r}+\frac{\delta\eta}{Ro}\right)+\frac{\delta\omega}{\tau}+\frac{\delta W_f(r,\theta)}{Ro}=\frac{1}{Re}\nabla^2\omega \tag{27}$$

$$\nabla^2\Psi=-\omega \tag{28}$$

$$u=-\frac{\partial\Psi}{\partial r} \tag{29}$$

$$v=\frac{1}{r}\frac{\partial\Psi}{\partial\theta} \tag{30}$$

subject to the no-slip and non-penetrating boundary conditions

$$\left.\frac{\partial\Psi}{\partial r}\right|_{R_{\text{out}}}=0,\quad \left.\frac{\partial\Psi}{\partial r}\right|_{R_{\text{in}}}=0 \tag{31}$$

and

$$\left.\frac{\partial\Psi}{\partial\theta}\right|_{R_{\text{out}}}=0,\quad \left.\frac{\partial\Psi}{\partial\theta}\right|_{R_{\text{in}}}=0 \tag{32}$$

3. DISCRETE APPROXIMATION

Equations (27)–(32) are numerically solved using a pseudo-spectral method. Spectral methods use a set of basis functions to expand the spatial variation of the vorticity field. The method is called pseudo-spectral for the treatment of the non-linear term. The standard pseudo-spectral method of computing non-linear terms is to compute derivatives in spectral space and then transform these result to physical space where the non-linearity is computed and then transform that result back into spectral space. Our choice of basis functions are Fourier series in the angular co-ordinate and Chebyshev polynomials in the radial [11].

In what follows we will typically be using a 'mixed space' formulation where the data are expanded in Fourier series in the θ direction and remain in physical space for the radial direction:

$$\omega(r_n,\theta,t)=\sum_{m=-N_\theta/2-1}^{N_\theta/2-1}\omega_m(r_n,t)\mathrm{e}^{\mathrm{i}m\theta} \tag{33}$$

We will use the notation ω_m to refer to the mth radial function in the expansion. The sum of these functions evaluated at the radial grid points (r_n) provides all the information about the flow at a given time. The streamfunction Ψ_m is decomposed similarly.

With this expansion the derivatives are obtained analytically. To obtain the coefficients for the derivative with respect to θ we simply multiply by the Fourier mode, i.e. $\partial\omega_m/\partial\theta=\mathrm{i}m\omega_m$. To take derivatives in the radial direction we make use of the well-known recursion relationship between the Chebyshev coefficients and the coefficients for the derivative. Since we will work with the data in mixed space we will create a derivative matrix operator that combines

the recursion relationship with the Chebyshev transform. The functions, ω_m, are vectors of vorticity data at each collocation point for a given Fourier mode. The derivative matrix, D, when operating on these vectors, returns the derivative of the function [12]. Numerical round-off error when using the Chebyshev derivative matrix is considered in Section 5. We note that similar numerical formulations have been used in related work on rotating annular flows [10, 13, 14].

3.1. Boundary conditions

In the mixed Fourier-physical space representation our boundary conditions on the functions from Equation (33) become

$$\left.\frac{\mathrm{d}\Psi_m(r)}{\mathrm{d}r}\right|_{R_{\mathrm{out}}} = 0, \quad \left.\frac{\mathrm{d}\Psi_m(r)}{\mathrm{d}r}\right|_{R_{\mathrm{in}}} = 0 \tag{34}$$

and

$$\mathrm{i}m\Psi_m(R_{\mathrm{out}}) = 0, \quad \mathrm{i}m\Psi_m(R_{\mathrm{in}}) = 0 \tag{35}$$

We find that for the $m = 0$ mode the latter boundary condition will always be satisfied; we require an additional equation to determine the value of $\Psi_{m=0}$.

The boundary condition for Ψ is related to the mean flow rate around the annulus (i.e. the speed and width of the jet). We define the mean flow rate around the annulus as the mean θ velocity, integrated from the inner to the outer radius. Using the fact that only the $m = 0$ Fourier mode corresponds to the mean in the θ direction we define the total flow rate, Q, to be

$$Q(t) = \int_{R_{\mathrm{in}}}^{R_{\mathrm{out}}} u_{m=0}\,\mathrm{d}r = -\int_{R_{\mathrm{in}}}^{R_{\mathrm{out}}} \frac{\partial \Psi_{m=0}}{\partial r}\,\mathrm{d}r = -\Psi_{m=0}(R_{\mathrm{out}}) + \Psi_{m=0}(R_{\mathrm{in}}) \tag{36}$$

The streamfunction can only be determined up to a constant, therefore we can arbitrarily define the value of Ψ to be zero at the inner boundary.

$$\Psi_{m=0}(R_{\mathrm{out}}) = -Q, \quad \Psi_{m=0}(R_{\mathrm{in}}) = 0 \tag{37}$$

The zeroth order velocity obeys the conservation of mass equation (refer back to Equations (8)–(10))

$$\mathrm{i}mu_m = -\frac{\partial r v_m}{\partial r} \tag{38}$$

In what follows we assume quantities refer to the zeroth order unless denoted with a subscript 1 to indicate that we are discussing first-order terms. For the $m = 0$ mode, we find that the radial velocity, v, is a constant. Since the radial boundary condition is impenetrable, the $m = 0$ radial velocity is 0.

The conservation of mass equation for the first-order velocity, Equation (20), evaluated for the $m = 0$ mode becomes

$$\frac{1}{r}\frac{\partial r v_{1,m=0}}{\partial r} = \delta(w_1|_{z=0} - w_1|_{z=H})_{m=0} \tag{39}$$

Using the expressions for the vertical velocity provided in the previous section the above equation reduces to

$$\frac{1}{r}\frac{\partial r v_{1,m=0}}{\partial r} = \frac{\delta}{Ro} W_{f,m=0} + \frac{\delta \omega_{m=0}}{\tau} \tag{40}$$

which can be integrated to give

$$v_{1,m=0} = \frac{\delta}{r\,Ro}\int_{R_{\text{in}}}^{r} \tilde{r} W_{f,m=0}\,\mathrm{d}\tilde{r} + \frac{\delta}{r\tau}\int_{R_{\text{in}}}^{r} \tilde{r}\omega_{m=0}\,\mathrm{d}\tilde{r} \tag{41}$$

The θ momentum equation (11) evaluated at the $m=0$ mode to provide the total flow around the annulus.

$$\frac{\partial u_{m=0}}{\partial t} + \left(\frac{u}{r}\frac{\partial u}{\partial \theta} + v\frac{\partial u}{\partial r} + \frac{uv}{r}\right)_{m=0} + v_{1,m=0} = \frac{1}{Re}\frac{\partial}{\partial r}\left(\frac{1}{r}\frac{\partial r u_{m=0}}{\partial r}\right) \tag{42}$$

which is rewritten as

$$\frac{\partial u_{m=0}}{\partial t} + \left(\frac{1}{r^2}\frac{\partial r^2 uv}{\partial r}\right)_{m=0} + v_{1,m=0} = \frac{1}{Re}\frac{\partial}{\partial r}\left(\frac{1}{r}\frac{\partial r u_{m=0}}{\partial r}\right) \tag{43}$$

where Equation (41) is used to evaluate the above expression for the first-order velocity.

4. TIME-STEP SCHEME

Now we discuss the procedure to solve the quasi-geostrophic equations in the annular geometry with the boundary conditions described above. For convenience, let us rewrite the QG equation in the following form:

$$\frac{\partial \omega}{\partial t} = B + \frac{1}{Re}\nabla^2 \omega \tag{44}$$

where the combination of non-linear, forcing and Ekman pumping terms are written as

$$B = -\frac{u}{r}\frac{\partial \omega}{\partial \theta} - v\left(\frac{\partial \omega}{\partial r} + \frac{\delta \eta}{Ro}\right) - \frac{\delta W_f}{Ro} - \frac{\omega \delta}{\tau} \tag{45}$$

We will solve Equation (44) using a fractional step scheme. We start each step by explicitly integrating the non-linear term across the time step, updating the values of vorticity, and follow by implicitly integrating the viscous diffusion operator. We use the Adams–Bashforth technique for the non-linear step and the backward Euler method for the linear diffusion step. We calculate B in Equation (45) using the pseudo-spectral approximation described in Section 3.

We take the fractional step and integrate the non-linear and forcing components of vorticity forward in time using the Adams–Bashforth technique

$$\omega_m^{k+1/2} = \omega_m^k + \frac{\Delta t}{2}(3B_m^k - B_m^{k-1}) \tag{46}$$

where k refers to the time step and $\frac{1}{2}$ refers to the fractional step.

Since integrating terms with ∇^2 operators are unstable unless Δt is very small, we use a fully implicit backward Euler technique for stability

$$\frac{\omega_m^{k+1} - \omega_m^{k+1/2}}{\Delta t} = \frac{1}{Re} \nabla^2 \omega_m^{k+1} \tag{47}$$

Equation (47) holds true for each Fourier mode, m, independently. Taking the diffusion step requires the inversion of a Helmholtz-type operator at each time step, for each Fourier mode. We can rewrite the equation such that all terms on the right-hand side are known and we must solve for the current value of the vorticity function

$$\left(r \frac{\mathrm{d}}{\mathrm{d}r} \left(r \frac{\mathrm{d}}{\mathrm{d}r} \right) - m^2 - r^2 \frac{Re}{\Delta t} \right) \omega_m^{k+1} = - \frac{Re}{\Delta t} r^2 \omega_m^{k+1/2} \tag{48}$$

Once the vorticity is known we must invert a Poisson operator in order to find the streamfunction

$$\left(r \frac{\mathrm{d}}{\mathrm{d}r} \left(r \frac{\mathrm{d}}{\mathrm{d}r} \right) - m^2 \right) \Psi_m^{k+1} = -r^2 \omega_m^{k+1} \tag{49}$$

For each Fourier mode we must solve two, one-dimensional boundary value problems in the radial direction.

4.1. Meeting boundary conditions

The difficulty with above vorticity-streamfunction formulations resides in the determination of the boundary conditions for vorticity. All boundary conditions are supplied for the streamfunction, but we cannot invert Equation (48) without boundary conditions for the vorticity. In order to satisfy all the boundary conditions on the streamfunction we will solve three independent well-posed problems and take the sum in a way such that the proper boundary conditions are imposed on the streamfunction. Further details of these decompositions in streamfunction-vorticity formulations are given by Peyret [15].

We will say that the final solution is expressed as

$$\Psi_m = \bar{\Psi}_m + E_1 \Psi_{1,m} + E_2 \Psi_{2,m} \tag{50}$$

and

$$\omega_m = \bar{\omega}_m + E_1 \omega_{1,m} + E_2 \omega_{2,m} \tag{51}$$

where the coefficients E_1 and E_2 are unknown. The m subscript reminds us that we must solve this boundary value problem for each Fourier mode.

The 'bar' problem is defined as

$$\left(r \frac{\mathrm{d}}{\mathrm{d}r} \left(r \frac{\mathrm{d}}{\mathrm{d}r} \right) - m^2 - r^2 \frac{Re}{\Delta t} \right) \bar{\omega}_m = - \frac{Re}{\Delta t} r^2 \omega_m^{k+1/2} \tag{52}$$

$$\left(r \frac{\mathrm{d}}{\mathrm{d}r} \left(r \frac{\mathrm{d}}{\mathrm{d}r} \right) - m^2 \right) \bar{\Psi}_m = -r^2 \bar{\omega}_m \tag{53}$$

with the Dirichlet boundary conditions

$$\bar{\omega}_m(r=R_{\text{in}})=0, \quad \bar{\omega}_m(r=R_{\text{out}})=0 \tag{54}$$

$$\bar{\Psi}_m(r=R_{\text{in}})=0, \quad \bar{\Psi}_m(r=R_{\text{out}})=0 \tag{55}$$

$$\bar{\Psi}_0(r=R_{\text{in}})=0, \quad \bar{\Psi}_0(r=R_{\text{out}})=-Q(t) \tag{56}$$

The '1' problem is defined as

$$\left(r\frac{\mathrm{d}}{\mathrm{d}r}\left(r\frac{\mathrm{d}}{\mathrm{d}r}\right)-m^2-r^2\frac{Re}{\Delta t}\right)\omega_{1,m}=0 \tag{57}$$

$$\left(r\frac{\mathrm{d}}{\mathrm{d}r}\left(r\frac{\mathrm{d}}{\mathrm{d}r}\right)-m^2\right)\Psi_{1,m}=-r^2\omega_{1,m} \tag{58}$$

with the boundary conditions

$$\omega_{1,m}(r=R_{\text{in}})=1, \quad \omega_{1,m}(r=R_{\text{out}})=0 \tag{59}$$

$$\Psi_{1,m}(r=R_{\text{in}})=0, \quad \Psi_{1,m}(r=R_{\text{out}})=0 \tag{60}$$

The '2' problem is defined as

$$\left(r\frac{\mathrm{d}}{\mathrm{d}r}\left(r\frac{\mathrm{d}}{\mathrm{d}r}\right)-m^2-r^2\frac{Re}{\Delta t}\right)\omega_{2,m}=0 \tag{61}$$

$$\left(r\frac{\mathrm{d}}{\mathrm{d}r}\left(r\frac{\mathrm{d}}{\mathrm{d}r}\right)-m^2\right)\Psi_{2,m}=-r^2\omega_{2,m} \tag{62}$$

with the boundary conditions

$$\omega_{2,m}(r=R_{\text{in}})=0, \quad \omega_{2,m}(r=R_{\text{out}})=1 \tag{63}$$

$$\Psi_{2,m}(r=R_{\text{in}})=0, \quad \Psi_{2,m}(r=R_{\text{out}})=0 \tag{64}$$

We select coefficients E_1 and E_2 in order to satisfy the Neumann condition on the streamfunction for each Fourier mode. Taking the derivative of the streamfunction and evaluating at the inner and outer boundary yields two equations for the two unknown values of E_1 and E_2:

$$\frac{\mathrm{d}\Psi_m}{\mathrm{d}r}=0=\left.\frac{\mathrm{d}\bar{\Psi}_m}{\mathrm{d}r}\right|_{R_{\text{in}}}+E_1\left.\frac{\mathrm{d}\Psi_{1,m}}{\mathrm{d}r}\right|_{R_{\text{in}}}+E_2\left.\frac{\mathrm{d}\Psi_{2,m}}{\mathrm{d}r}\right|_{R_{\text{in}}} \tag{65}$$

$$\frac{\mathrm{d}\Psi_m}{\mathrm{d}r}=0=\left.\frac{\mathrm{d}\bar{\Psi}_m}{\mathrm{d}r}\right|_{R_{\text{out}}}+E_1\left.\frac{\mathrm{d}\Psi_{1,m}}{\mathrm{d}r}\right|_{R_{\text{out}}}+E_2\left.\frac{\mathrm{d}\Psi_{2,m}}{\mathrm{d}r}\right|_{R_{\text{out}}} \tag{66}$$

Once the unknown values of E are found the solution of the three problems may be combined. Checking the definition of the '1', '2' and 'bar' problems shows that the final result satisfies all the boundary conditions and equations. We also note that the solution of the '1' and '2' problems can be done once at the beginning in a preprocessing step and stored for the remainder of the simulation.

4.2. *Mean flow, $m=0$ Fourier mode boundary condition*

The solution of the $m=0$, θ-momentum equation at each time step provides the current value of the flow rate, Q. This flow rate is used as the boundary condition on the streamfunction when solving the 'bar' problem. We follow the same time-stepping scheme that we applied for the QG equation, namely the Adams–Bashforth step followed by backward Euler:

$$u_0^{k+1/2} = u_0^k + v_{1,m=0} + \frac{\Delta t}{2}\left(3\,\frac{1}{r^2}\,\frac{\partial r^2 uv}{\partial r}^{k} - \frac{1}{r^2}\,\frac{\partial r^2 uv}{\partial r}^{k-1}\right)_0 \tag{67}$$

$$\left(r^2\,\frac{\mathrm{d}^2}{\mathrm{d}r^2} + r\,\frac{\mathrm{d}}{\mathrm{d}r} - I - r^2\,\frac{Re}{\Delta t}\right) u_0^{k+1} = -\frac{Re}{\Delta t}\,r^2 u_0^{k+1/2} \tag{68}$$

In the above equation we use the subscript 0 to refer to the $m=0$ mode.

Equation (67) is solved at the beginning of the time step along with the other non-linear terms. Once we solve Equation (68) with the boundary condition that $u_0=0$ on both the inner and outer radius we can integrate to compute the total flow rate. We can then proceed with solving the 'bar' problem where the flow rate is used as the boundary condition for the $m=0$ streamfunction equation.

4.3. *Matrix inversion: eigenvalue/vector decomposition*

Each of the above problems ('bar', '1', '2' and $m=0$) involves the inversion of a Helmholtz and Poisson-type operator. We will now detail the method of inverting the Helmholtz and Poisson problems, these matrix inversion methods are outlined by Boyd [11].

Given the definitions of the Chebyshev transform and the recursion relation that exists between coefficients for the derivatives, we can write the Poisson and Helmholtz equations as the matrix equations

$$\left(\Gamma D \Gamma D - \frac{Re}{\Delta t}\,\Gamma^2 - m^2 I\right)\omega_{\mathbf{m}} = -\frac{Re}{\Delta t}\,\Gamma^2 \omega_{\mathbf{m}} \tag{69}$$

$$(\Gamma D \Gamma D - m^2 I)\boldsymbol{\Psi}_{\mathbf{m}} = -\Gamma^2 \boldsymbol{\omega}_{\mathbf{m}} \tag{70}$$

where D represents the first derivative matrix operator, I is the identity matrix, Γ is a diagonalized matrix that contains the radius at the collocation points and $\boldsymbol{\Psi}_{\mathbf{m}}$ and $\omega_{\mathbf{m}}$ are vectors of the stream function and vorticity for Fourier mode, m. For the purposes of the remaining discussion in this section we generalize Equations (70) and (69) as

$$(M - m^2 I)\mathbf{f} = \mathbf{g} \tag{71}$$

where M is a matrix, and $\mathbf{f}$ and $\mathbf{g}$ are vectors ($\mathbf{g}$ is the known).

Before we invert this equation we will need to insert boundary conditions: note that in the 'bar', '1' and '2' problems we always enforce the value of the function, not the derivatives. The standard way to insert boundary conditions is to overwrite the rows of the matrix that set the values on the boundary, i.e. the first and last row of the matrix $(M - m^2 I)$. The reader should consult Trefethen [12] for details of inserting boundary conditions into matrix operators.

To invert the matrix equation efficiently, we will use the Haidevogel–Zhang decomposition [11]. This decomposition uses the fact that the matrices can be written as

$$M = E\Lambda E^{-1} \tag{72}$$

where E is the matrix of eigenvectors corresponding to the diagonal matrix of eigenvalues, Λ. This decomposition allows Equation (71) to be written as

$$E(\Lambda - m^2 I)E^{-1}\mathbf{f} = \mathbf{g} \tag{73}$$

which reduces to

$$(\Lambda - m^2 I)E^{-1}\mathbf{f} = E^{-1}\mathbf{g} \tag{74}$$

Finally, we can solve for f using

$$\mathbf{f} = E(\Lambda - m^2 I)^{-1}E^{-1}\mathbf{g} \tag{75}$$

In this form, the eigenvector and eigenvalue matrices (E, Λ and E^{-1}) are found once in a preprocessing step for both the Poisson and Helmholtz operators. At each time step, $\mathbf{f}$ can be found from a set of matrix vector-multiplications, an N^2 operation. Inverting the matrix $(\Lambda - m^2 I)$ is efficient since this matrix is diagonal.

4.4. Turbulence model

One of the well-known difficulties with turbulence simulations is the impossibility of resolving all the scales of motion in a high Reynolds number flow. In 3D turbulence, energy is known to follow a cascade to smaller scales; large eddies continually transfer their energy to smaller eddies until reaching a size that molecular viscosity is effective. In 2D turbulence the dominant energy cascade is to large scales; however, enstrophy cascades to smaller scales where it is dissipated by molecular viscosity. In geophysical applications the length scale where molecular viscosity is effective is several orders of magnitude smaller than the resolvable length scale of the simulation and we have no choice but to truncate the small scales in the numerical experiments. If we simply truncate the numerical approximation, the enstrophy cascade will have no mechanism by which to dissipate and small-scale flow structures will artificially accumulate [16]. Typically a model for small-scale motions is added so that the turbulent flow equations can be solved without numerical blow-up. Many turbulence models have been proposed for various different flows over the past several decades, for example, see Reference [17].

We elect to employ one of the simplest and most common turbulence models in two-dimensional simulations, hyperviscosity [17–21]. In a fully periodic simulation the hyperviscosity is mathematically equivalent to adding a high-order Laplacian to the governing equations; i.e.

$$\frac{\mathrm{D}\omega}{\mathrm{D}t} = B + \frac{1}{Re}\nabla^2\omega + (-1)^{n+1}\nu_{\mathrm{h}}(\nabla^2)^n\omega \tag{76}$$

where ν_{h} is the coefficient of hyperviscosity. In a fully periodic spectral simulation, the hyperviscosity operator can be written as

$$(-1)^n\nu_{\mathrm{h}}(\nabla^2)^n = -\nu_{\mathrm{h}}\left(\frac{|\mathbf{k}|}{k_{\max}}\right)^{2n} \tag{77}$$

where we have normalized the absolute value of two-dimensional wave number, $|\mathbf{k}|$, by the maximum wave number in the simulation $k_{\max}$ [18, 20, 21]. We solve the hyperviscous term implicitly using the backward Euler method when implementing this term in our governing equations. This integration method results in the following filter for the coefficients of the two-dimensional Fourier transform

$$\sigma_{k_x,k_y} = \frac{1}{1 + \nu_h(|\mathbf{k}|/k_{\max})^{2n}} \tag{78}$$

The hyperviscosity term acts like a low-pass filter to damp the highest Fourier modes and leave the lower modes unchanged.

When using a hyperviscous term with Chebyshev spectral methods, one would require additional (and artificial) boundary conditions when solving Equation (76). To preserve the boundary conditions we employ the method presented by Boyd [22] that maintains the properties of Laplacian-based hyperviscosity while not effecting the boundary conditions. Boyd's method uses a carefully selected and spatially dependent viscosity coefficient that decays to zero at the walls and therefore the method does not require additional boundary conditions. The interested reader should consult [22] for details on the implementation of this method of hyperviscosity; it is very similar to the expressions provided above for the fully periodic flow.

To determine the value for the power of the 'Laplacian' and the hyperviscosity coefficient we employ the method described in Reference [18] where the power and coefficient are determined by the flow itself. The method is analogous to the Smagorinsky model for large eddy simulation (LES) [17]. In the Smagorinsky model, the effective viscosity is related to the local rate of strain in the flow. We use the method discussed in Reference [18] to compute a hyperviscosity coefficient that is proportional to the volume averaged rate of strain. Smith's [18] method for determining the hyperviscosity coefficient is similar to the method described in Reference [19] that bases the magnitude of the hyperviscosity coefficient on the root-mean-squared vorticity or the method of Reference [20] that uses the time-step size as determined by the Courant condition to obtain the hyperviscosity coefficient. All three methods are using the flow to determine a characteristic time scale over which to 'smooth' the small-scale fluctuations. The power for the hyperviscous term is adaptive according to the algorithm of Reference [18], but is typically $n = 8$ or higher.

The primary results of Section 6 were tested and found to be insensitive to the exact details of the model. We tried fixed powers for the hyperviscous power and found that the conclusions of this paper were reasonably insensitive to the choice; i.e. $n = 8$ provided similar results as the variable power method. The precise method of determining the hyperviscosity coefficient did not have a major impact on the general qualities of the solution. We independently tried methods for determining the hyperviscous Reynolds number using the recommendations of References [18–20]; which all base the magnitude of the hyperviscosity on a measure of flow time scale. We found that the general results of this paper were unaffected by the precise algorithm used. Flows computed at different spatial resolutions have similar large-scale behaviours with our implemented method, indicating that the choice of hyperviscosity is suitable for our flows.

This simple hyperviscous filtering model may not be acceptable; however, *all* two-dimensional turbulence simulations must use some form of 'turbulent viscosity' [9]. In forced two-dimensional flows it is often assumed that there is not much influence of small-scale motions

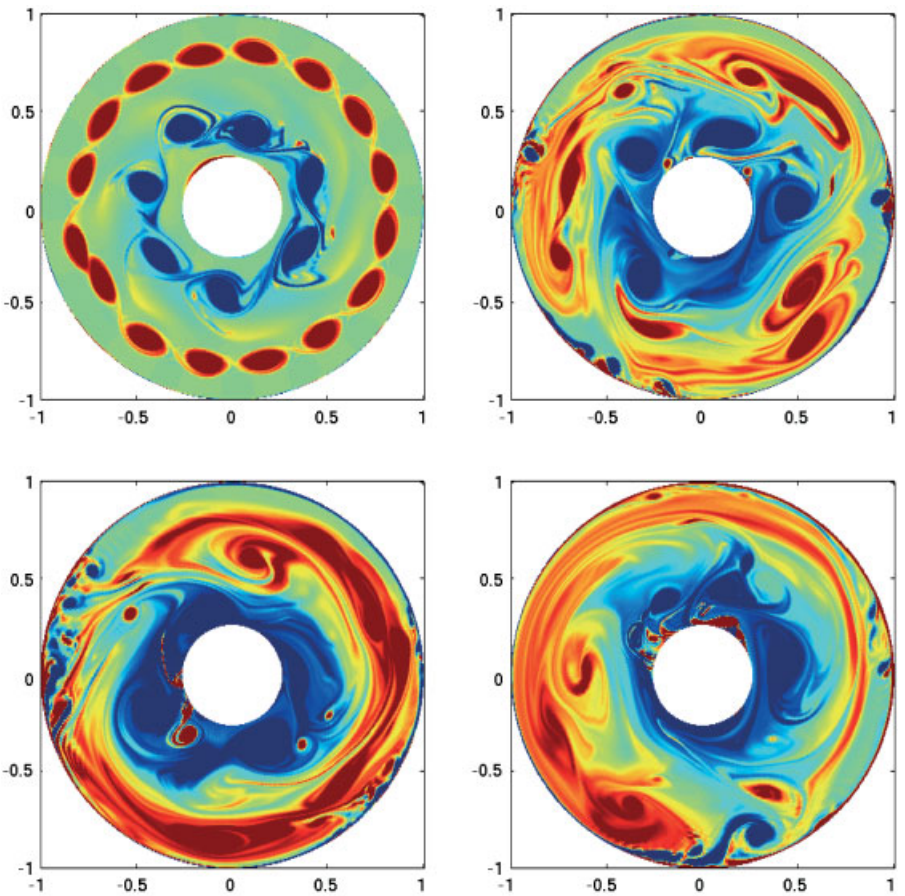

Plate 1. Snapshot of vorticity fields at various times. Each forcing ring creates localized vorticity directly above the inlet and outlet holes. In this configuration, a sharp counter-rotating jet is formed between the forcing rings and the large velocity gradient at the boundary of the jet causes the flow to roll up into a ring of vortices. These vortices then begin to advect each other around the domain and go fully turbulent. The simulation is run for about 40 s of real time with about 10 seconds between snapshots (with the first one occurring 10 seconds into the simulation). The tank is rotating at 1.75 Hz with a pumping rate of 150 cm^3/s. Simulations are performed on a 512^2 grid.

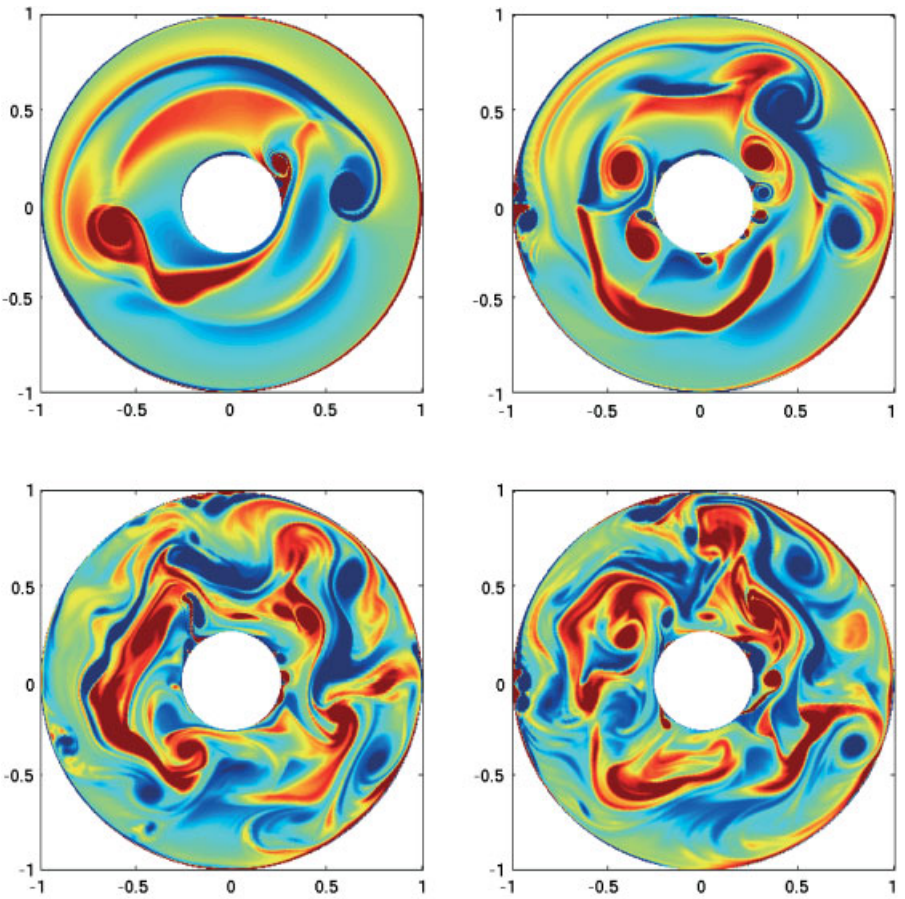

Plate 2. Snapshot of vorticity fields at various times using the semi-circle forcing. The simulation is run for about 135 seconds of real time with the snapshots taken at 8, 16, 45 and 135 seconds going left to right then down. The tank is rotating at 1.75 Hz with a pumping rate of 150 cm^3/s in order to compare to experiments. Simulations are performed on a 512^2 grid. Large vortices are created at the transition between sources and sinks. As in the experiment the beta-plane causes cyclones to move radially inward and anti-cyclones to move radially outward.

acting across the forcing scale and therefore any low-pass filter is a reasonable closure model. On the other hand, some researchers have noted serious errors with the hyperviscosity approach that questions the validity of many two-dimensional turbulence simulations [23]; however, these conclusions were based on a ∇^4 damping. Ultimately, the validity of the turbulence model in our flow will be determined by the agreement with the experimental data.

In addition to using a turbulence closure model for the stability of the simulations, there is also the question of whether a model for turbulent Ekman pumping is required; we used a laminar result based on molecular viscosity in Equation (22). Early work by Ekman proposed using an effective turbulent eddy-viscosity [24] and many models since have been proposed and tested for the dissipation in turbulent Ekman layers [25]. In our case, we use the molecular viscosity in the Ekman dissipation term for two reasons. One reason is that the experiments validate that the flow remains very two dimensional across the height of the annulus at the small scales of our simulation [7]; therefore, the Ekman pumping based on a two-dimensional flow assumption is reasonably valid even at the small scales. The second practical reason is that the Ekman spin down time is long (30 s) compared to the typical turnover time of the vortices (1 s). In this experimental geometry, the Ekman dissipation has little impact on the final results. The dissipation term is included in the formulation as it is crucial for determining the steady-state size of vortices in atmospheric simulations where the geometry of the boundary conditions does not set the size of vortices and jets [9].

5. ALGORITHM TESTING AND PERFORMANCE

The algorithm was tested on grids of different resolutions: 256, 512 and 1024. Since the flows are fully turbulent and non-linear it is not expected that any deterministic solution is truly meaningful on any grid (i.e. we cannot predict the weather very far in the future). Thus, we cannot simply compare vorticity fields at a given instant on different grids and expect them to be identical. We require that on different grids the simulation can capture the same statistical distributions, mean properties and the basic qualities of the flow. To compare the solutions on different grids we use mean quantities (the strength of the jets created), the transition time from a sharp jet to rolled-up vortices (we will see this in the results section), the general qualities of the flow (size of vortices and behaviour at the wall) and the statistical distributions. We will discuss specific comparisons in Section 6. We found that the simulation provides reliable results on all the grids tested. We do find finer filamentation of vorticity and smaller vortices generated and ejected from the wall at higher resolution. However, it seems that the basic transport of energy from the small-scale forcing to the large-scale vortices that dominate the flow are not heavily influenced by the amount of small-scale dissipation.

Since the simulations we are performing require high resolution and long integration times, we need the algorithms to scale efficiently, both as the grid size is increased and the number of processors is varied. The total algorithm is composed of various matrix operations: some scale with the total system size ($N_r N_\theta$), the FFT of the entire data set scales as $N_r N_\theta \operatorname{Log}_2(N_\theta)$ and the solving of the Poisson (and Helmholtz)-type equations scale as $N_\theta N_r^2$. The above relations are only scalings, and the total algorithm cost will depend on how many of each of these operations are done (i.e. how many Helmholtz, FFTs, etc). In Figure 1, we show the normalized total computation time as the computational grid is increased: in this figure

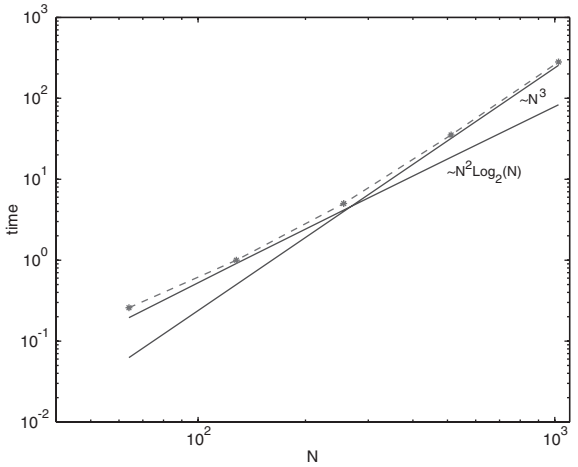

Figure 1. Scaling of the algorithm as the system size is changed. The number of grid points is always square in this figure. We show actual data from single processor simulations and compare to scalings expected from the FFT and the Helmholtz/Poisson solver. When the number of grid points is large the algorithm is dominated by solving the Poisson and Helmholtz equations. This operation scales as $N_\theta N_r^2$, or N^3 on the square grid.

the domain remains square ($N_r = N_\theta$). We see that at fine resolution, the algorithm time is dominated by N^3 operations, as we would expect.

The algorithm has been implemented for parallel architectures using the message passing interface (MPI) protocols [26]. The solution of the Helmholtz and Poisson equations are independent for each Fourier mode, so we parallelize the data by giving each processor an equal-sized set of Fourier modes to work with. This decomposition lets each processor work independently when solving the Helmholtz/Poisson steps and perfect scaling is trivial to obtain. Perfect scaling means that doubling the number of processors would half the total computation time. We easily achieve perfect scaling on the most expensive part of the calculation. The only step in the code that has any cross-processor communication is the FFT in the θ direction. Good parallel performance with this algorithm is possible since many packages codes exist to perform the parallel FFT.

The use of Chebyshev derivative matrices can be susceptible to round-off errors the resolution is high [27]. Many round-off error problems are confined to the calculation of the derivative during the computation of the non-linear terms. We follow the recommendations of References [15, 27] to minimize the effect of round-off error in the construction of the derivative operator. We tested the computation of the derivative in the local computing environment and found that typical relative errors were less than 10^{-8} when using these round error control methods. In general, the effects of round-off error are much less pronounced in the solution of differential equations [15, 28]. Specifically, the computation of the eigenvalues for use in the solution of the Helmholtz problem is not susceptible to round-off error. The precision of the computation of the eigenvalues is controlled by the condition number of the eigenvector matrix not the condition of the second derivative matrix (i.e. the condition of E not M in Equation (72)) [15]. The eigenvector matrix E is well conditioned. Again, the

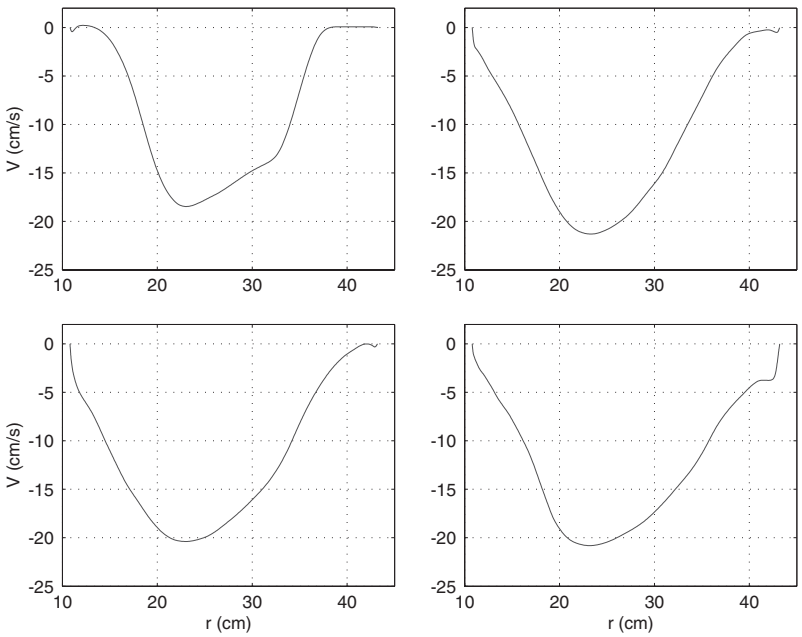

Figure 2. Mean radial velocity profiles of the counter-rotating jet corresponding to the snapshots in Plate 1. The jet flows in the opposite direction of the tank rotation with a velocity of approximately 20 cm/s. Initially the jet is confined between the forcing rings. As the edge of the sharp jet becomes unstable, the fully turbulent flow encompasses the whole domain. Marcus and Lee [10] showed why care must be taken when comparing the mean flow profiles; however, the simulation should reproduce these basic flow properties.

solution of the Helmholtz and Poisson problem was tested on several known solutions and was confirmed to have no significant influence from round-off error.

6. RESULTS

The objective of this section is to demonstrate typical results and show that the simulation method is capable of capturing the dominant features of the experimental data. This paper is primarily meant to present the methods, algorithms and early results of testing; more detailed analysis of the comparisons between theory and experiment will be conducted in future work.

First we simulate the data from the counter-rotating jet configuration [7]. In this experiment, fluid is pumped into the domain at an inner forcing ring and removed at the outer forcing ring. The inner ring is located at a radius of 18.9 cm and the outer ring is located at 35.1 cm. The rotation rate of the tank is 1.75 Hz with a pumping rate of 150 cm^3/s. The simulation is run for about 40 s; 70 rotations of the tank. Some sample results from these simulations are shown in Plate 1 and Figure 2. The conditions were selected to match the documented experimental data [7].

The vertical flow at the inlets generates anti-cyclonic vorticity while the vertical flow at the outlets generates cyclonic vorticity. The localized vorticity above the forcing creates a strong counter-rotating jet between the inner and outer ring. The large velocity gradients that initially develop at the edge of the jet are unstable and roll up into the vortex rings as seen in the first snapshot of Plate 1. The development of the most unstable mode in these jets is discussed in detail by Marcus and Lee [10]. Our simulations go beyond this previous work and capture the development, dynamics and eventual steady state of the turbulent flow.

Plate 1 shows instantaneous vorticity fields at different times and Figure 2 shows the mean flow of the jet as a function of radius at the corresponding times. At early times we find that the jet is confined between the forcing rings. As the sharp velocity gradient goes unstable, vortices roll up at the interface. The turbulent vorticity fields in the simulation have many of the same qualities as the experimental results. Long-lived cyclones stay in the outer region of the annulus where they have the same sign as the background shear. Marcus [29] showed that QG vortices must have the same sign vorticity as their background shear otherwise they are quickly dissipated. For the same reason the inner part of the annulus is dominated by anti-cyclones. The magnitude of the jet velocity agrees with the experimentally recorded values of 20 cm/s.

We also find that small vortices are generated at the wall when large coherent vortices sweep by. These small vortices are injected into the flow where they merge with like-signed vortices. Sequences of vorticity images show that cyclones generated at the inner boundary and are ejected across the jet to the outer part of the annulus where they are stable. These processes were also observed experimentally and explained extensively in the work of Baroud *et al.* [7] as an example of non-local (in wave number sense) energy transfer. The simulation demonstrates the ejection of vortices at the wall and their migration into the bulk flow.

In addition to the mean and qualitative properties of the flow, the simulation may be also used to predict the turbulent statistics of the counter-rotating jet. Figure 3 shows normalized velocity difference probability distribution function (PDF) for different separations [17]. The simulated 'measurements' are taken along the flow centreline to emulate the experimental hot-film measurements. The simulated statistics are in good agreement with the experimental results [7]. The fact that the experimental PDF for different spacings normalize to a single curve was used as evidence for two-dimensional, self-similar flow. The agreement between the experiments and simulations helps to demonstrate that the strength and frequency of the turbulent vortices are well modelled by our simulations. The non-Gaussian tails on the distribution are a result of coherent vortices [30].

Next we demonstrate a different configuration of forcing holes to simulate the experimental data of Aubert *et al.* [8]. The forcing ring is now centred between the inner and outer radius. The lower half (semi-circle) of the forcing ring is taken to be inlets while the upper half is taken to be outlets. This forcing configuration results in a flow with three robust zonal flows: a co-rotating jet is located along the centre where the forcing occurs and two counter-rotating jets are located along the inner and outer radius of the annulus.

Plate 2 shows vorticity fields at different instances in times while Figure 4 shows the mean velocity as a function of radius. Early in the simulation we see a large cyclone and anti-cyclone form at the locations where the forcing transitions from sources to sinks. The sloping lower boundary (beta-effect) tends to push the cyclone inward and the anti-cyclone outward. While strong cyclones occasionally venture toward the outer radius, on average cyclones spend much more time near the inner radius where their existence is stable. The magnitude of the

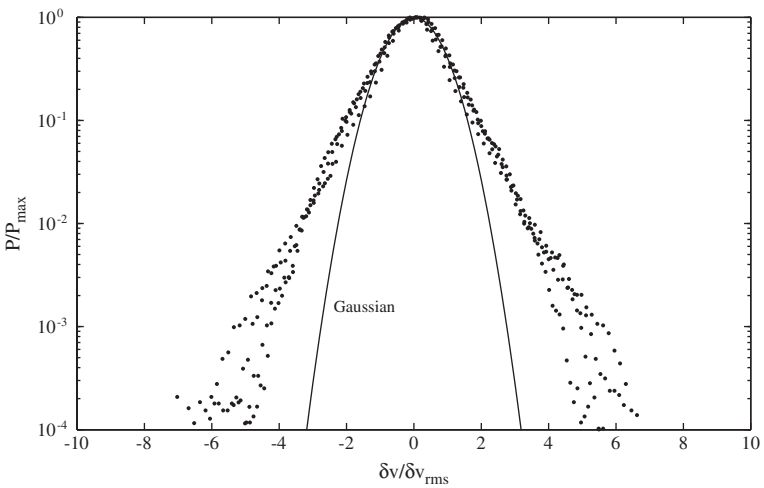

Figure 3. Normalized probability distribution function of velocity differences taken along the centreline from the counter-rotating configuration. The simulated data is presented to match Figure 8 of Reference [7]; good quantitative agreement exists between the simulated and experimental PDF. The figure is displaying the normalized PDFs computed at separations of 2.3, 4.6, 9.2, 12.7 and 17.3 cm. The simulated data is taken from the configuration of Plate 1 and Figure 2.

zonal velocities agrees well with the reported experimental data [8] of approximately 2 cm/s. As with the previous configuration the simulated properties of the jet flow agree with the experimental observations.

Figure 5 compares the simulated PDF of vorticity in the semi-circle forced flow to a theory based on non-extensive statistical mechanics. This theory has been shown to predict the experimental data quite well. The experimental probability density functions show broad tails with significant departure from Gaussian statistics [6]. Our simulations show quantitative agreement with the experimental results, with the exception of a slight asymmetry in the distribution toward anti-cyclones. The quality of the simulated statistics are limited by the relatively short run times of numerical experiments—it is difficult to assess if the asymmetry in the data is due only to poor statistics. In future work, we hope to run longer simulations and conduct more detailed comparisons of the simulated statistical behaviour. The agreement with the experimental statistical data demonstrates the quantitative utility of the simulation results.

In the cases presented thus far we can compute the Rossby number of the final flow field to verify that the simulation is consistent with the QG approximation. Baroud *et al.* [7] used the definition of $Ro \equiv \omega_{\text{rms}}/2\Omega$ to classify the two dimensionality of the flows. Using this definition, our simulation predicts $Ro \sim 0.12$ in the counter-rotating jet configuration and $Ro \sim 0.08$ in the semi-circle forcing. These Rossby numbers are consistent with experimental findings and place the flow in the two-dimensional, quasi-geostrophic regime [7].

We tested the results of presented herein on a lower resolution grid (256) as well as tested a short period of the simulations with a higher resolution (1024). The first snapshot in Plate 1 appears the same for the three different grid resolutions, with some noticeable differences in

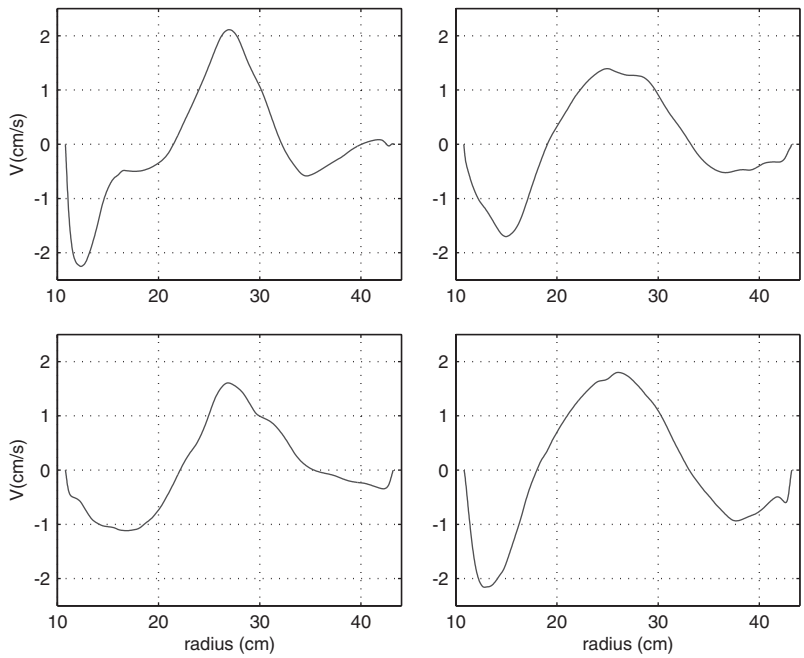

Figure 4. Mean velocity profiles with the semi-circle forcing corresponding to the instances shown in Plate 2. The forcing creates three zones with velocities on the order of 1–2 cm/s. The co-rotating jet is centred at the forcing ring. Anticyclones prefer the outer half of the annulus while cyclones prefer the inner half where the vortices are stable to the background shear. The profiles agree with the experimental data.

the vorticity field developing by the second image. As the flow becomes fully turbulent by the third image, the 256 and 512 solutions depart when comparing the instantaneous vorticity fields (the 1024 was not integrated for this long period). However, the bulk properties of the flow are preserved; vortices have similar sizes, mean flows are the same and turbulent statistics are well captured. The results presented in this section are the same when generated by the 256 resolution simulation. We find that the higher resolution simulations provide more vorticity filamentation and capture more detailed vorticity structure generated at the wall. Owing to the time it takes to evolve to a turbulent steady state, it is not practical to run 1024 grid calculations to collect statistics. The results of the testing indicated that a 512 grid is adequate for these simulations. The good comparisons between the simulations and the experiments presented in this section validate that the simulations are robust in capturing the features of interest; despite the limitations of the hyperviscosity model.

7. CONCLUSIONS

We have developed an algorithm for solving the two-dimensional quasi-geostrophic equations on parallel architectures using MPI. The numerical simulations are modelling laboratory experiments in order to understand basic turbulent processes in rotating flows. The algorithm

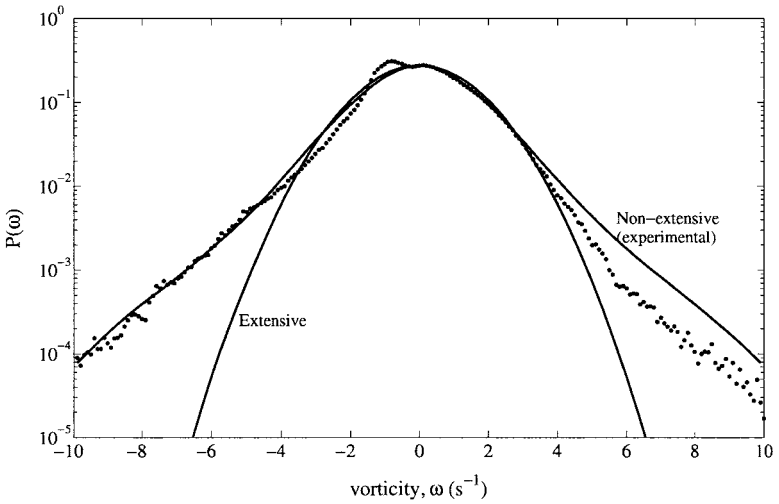

Figure 5. Comparisons of the vorticity probability distribution function of the simulation (points) and a theory based on a non-extensive statistical mechanics. The theory was shown to predict experimental data (solid) extremely well [6]. We also show the extensive (or Gaussian) fit to the simulated data for comparison. The simulated data agrees well with the non-extensive fit; however, the simulation shows a slight asymmetry to anti-cyclones that was not present in the experimental data. The simulated data is taken from the semi-circle forcing of Plate 2 and Figure 4.

has been developed and tested yielding results in good agreement with experimental data. These results indicate that the simulation will be useful in predicting laboratory results before making system changes. We hope to use such computations to design future experiments that will demonstrate different zonal flow behaviours.

ACKNOWLEDGEMENTS

The author began this work while spending the summer at the Centre for Non-Linear Dynamics at the University of Texas as a visitor in the laboratory Professor Harry Swinney. The author would like to thank Harry Swinney, Sunny Jung and Eran Sharon at CNLD for a pleasant stay and many helpful discussions. Computations were performed on the Blue Horizon at the San Diego Supercomputing Centre and Longhorn at Texas Advanced Computing Centre. Resources were allocated through the NPACI program of NSF.

REFERENCES

1. Pedlosky J. *Geophysical Fluid Dynamics.* Springer: Berlin, 1992.
2. Sommeria J, Meyers SD, Swinney HL. Laboratory model of a planetary eastward jet. *Nature* 1989; **337**: 58–61.
3. Sommeria J, Meyers SD, Swinney HL. Laboratory simulation of Jupiter's Great Red Spot. *Nature* 1989; **331**: 689–693.
4. Solomon TH, Halloway WJ, Swinney HL. Shear flow instabilities and Rossby waves in barotropic flow in a rotating annulus. *Physics of Fluids* 1993; **5**:1971–1982.
5. Baroud CN, Plapp BB, She ZS, Swinney HL. Anomalous self similarity in a turbulent rapidly rotating fluid. *Physical Review Letters* 2002; **88**:114501-1-4.
6. Jung S, Storey BD, Aubert J, Swinney HL. Energy-enstrophy model for two-dimensional Euler flows. 2003; (in press).

7. Baroud CN, Plapp BB, Swinney HL, She ZS. Scaling in three-dimensional and quasi-two-dimensional rotating turbulent flows. *Physics of Fluids* 2003; **15**:2091–2104.
8. Aubert J, Jung S, Swinney HL. Observations of zonal flow created by potential vorticity mixing in a rotating fluid. *Geophysical Research Letters* 2002; **9**:1876–1879.
9. Marcus PS, Kundu T, Lee C. Vortex dynamics and zonal flows. *Physics of Plasmas* 1998; **7**:1630–1640.
10. Marcus PS, Lee C. A model for eastward and westward jets in laboratory experiments and planetary atmospheres. *Physics of Fluids* 1998; **10**:1474–1489.
11. Boyd JP. *Chebyshev and Fourier Spectral Methods*. Dover: New York, 2001.
12. Trefethen LN. *Spectral Methods in MATLAB*. SIAM: Philadelphia, PA, 2001.
13. Plaut E, Busse FH. Low Prantl-number convection in a rotating cylindrical annulus. *Journal of Fluid Mechanics* 2002; **464**:345–363.
14. Chen CX, Zhang K. Nonlinear convection in a rotating annulus with a finite gap. *Geophysical and Astophysical Fluid Dynamics* 2002; **96**:499–518.
15. Peyret R. *Spectral Methods with Application to Incompressible Viscous Flow*. Springer: Berlin, 2002.
16. Frisch U. *Turbulence*. Cambridge University Press: Cambridge, MA, 1995.
17. Pope S. *Turbulent Flows*. Cambridge University Press: Cambridge, MA, 2000.
18. Smith SA, Hammett GW. Eddy viscosity and hyperviscosity in spectral simulations of 2D drift wave turbulence. *Physics of Plasmas* 1997; **4**:978–990.
19. Marcus PS, Lee C. Jupiter's Great Red Spot and zonal winds as a self-consistent, one-layer, quasigeostrophic flow. *Chaos* 1994; **4**:269–286.
20. Borue V, Orszag SA. Numerical study of three-dimensional Kolmogorov flow at high Reynolds number. *Journal of Fluid Mechanics* 1996; **306**:293–323.
21. Basdevant C, Legras B, Sadourny R, Beland M. A study of barotropic model flows: intermittency, waves, and predictability. *Journal of Atmospheric Science* 1981; **38**:2305–2326.
22. Boyd JP. Two comments on filtering (artificial viscosity) for Chebyshev and Legendre spectral and spectral element methods: preserving boundary conditions and interpretation of the filter as diffusion. *Journal of Computational Physics* 1998; **143**:283–288.
23. Yao HB, Zabusky NJ, Dritschel DG. High gradient phenomena in 2-D vortex interactions. *Physics of Fluids* 1995; **7**:539–548.
24. Ekman VW. Eddy-viscosity and skin friction in the dynamics of winds and ocean currents. *Memoirs of the Royal Meteorological Society* 1928; **2**:161–172.
25. Caldwell VW, Van Atta CW, Helland KN. A laboratory study of the turbulent Ekman layer. *Geo*, *Fluid Dynamics* 1972; **3**:125–160.
26. Gropp W, Lusk E, Skjellum A. *Using MPI—2nd Edition*: *Portable Parallel Programming with the Message Passing Interface*. MIT Press: Cambridge, MA, 1999.
27. Bayliss A, Class A, Matkowsky BJ. Roundoff error in computing derivatives using Chebyshev differentiation matrix. *Journal of Computational Physics* **116**:160–172.
28. Breuer KS, Everson RM. On the errors incurred calculating derivatives using Chebyshev polynomials. *Journal of Computational Physics* **99**:55–67.
29. Marcus PS. Jupiter's Great Red Spot and other planetary vortices. *Annual Review of Astronomy and Astrophysics* 1993; **31**:523–573.
30. Farge M, Schneider K, Kevlahan N. Non-Gaussianity and coherent vortex simulation for two-dimensional turbulence using an adaptive orthogonal wavelet basis. *Physics of Fluids* 1999; **11**:2187–2201.

